ARTICLE INFO
Article ID: 03-14-02-0018

doi:10.4271/03-14-02-0018

Effects of Ambient Oxygen and Density on Primary Soot Size under Diesel-Like Conditions Using a Lagrangian Soot Tracking Model

Jiun Cai Ong,[1,2] Kar Mun Pang,[1] Jens Honore Walther,[1,3] Jee-Hou Ho,[2] and Hoon Kiat Ng[2]

[1]Technical University of Denmark, Denmark
[2]University of Nottingham Malaysia Campus, Malaysia
[3]ETH Zürich, Switzerland

Abstract

This article investigates the effect of ambient oxygen (O_2) levels and ambient density on the primary soot size under diesel engine-like conditions via the Lagrangian soot tracking (LST) method. The numerical studies and soot analysis are carried out for an *n*-heptane spray flame in the Sandia constant volume combustion chamber. Numerical studies are carried out at two O_2 levels of 15% and 12%, as well as two ambient densities of 14.8 kg/m^3 and 30 kg/m^3. The LST model involves treating the soot particles formed in the spray flame as Lagrangian particles, and their individual soot information is stored. Based on the primary soot size distribution for soot particles in the core of the spray jet, an increase in ambient density from 14.8 kg/m^3 to 30 kg/m^3 is shown to increase the peak and mean soot size by a factor of 1.5. Furthermore, the peak and mean primary soot size decreases with decreasing O_2 levels from 15% to 12%. The larger primary soot size at higher O_2 levels and ambient densities can be attributed to the higher net growth rate experienced by the soot particles. At low density, the span of the soot cloud is shorter O_2 level is low. In contrast, the high-density cases show a comparable soot cloud span at both O_2 levels before steady-state is reached. Soot age is introduced to predict the soot residence time in the spray flame. The results show that the soot residence time is dependent on both the span of the soot cloud and the initial onset location of the soot formed.

History

Received: 07 Aug 2020
Revised: 23 Oct 2020
Accepted: 14 Dec 2020
e-Available: 10 Mar 2021

Keywords

Lagrangian soot tracking, Primary soot, Soot age, Soot size, Diesel spray

Citation

Ong, J., Pang, K., Walther, J., Ho, J. et al., "Effects of Ambient Oxygen and Density on Primary Soot Size under Diesel-Like Conditions Using a Lagrangian Soot Tracking Model," *SAE Int. J. Engines* 14(2):2021, doi:10.4271/03-14-02-0018.

ISSN: 1946-3936
e-ISSN: 1946-3944

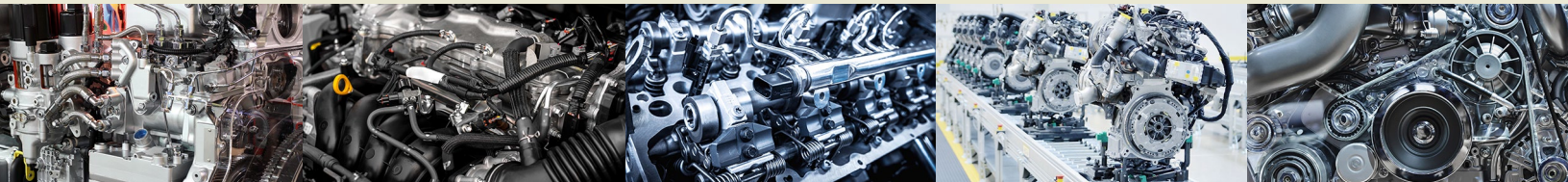

1. Introduction

Soot is one of the most distinctive and problematic emissions of diesel engines due to its complex formation and oxidation processes. Soot particles are normally formed as fractal open-structured agglomerates with large quantities of nanosized primary particles via incomplete combustion of hydrocarbon fuels [1, 2]. The morphological characteristics and nanostructural properties of combustion-generated soot particles are of paramount importance because they are closely linked to the formation of primary soot particles and soot oxidative reactivity [3]. Furthermore, ultrafine particle emissions from incomplete combustion are harmful to human health [4, 5]. This concern has led to the legislation of Euro 5/6, which aims to reduce soot mass and particle number emissions [6, 7]. Driven by the stringent legislations for pollutant emissions, detailed analysis of soot morphology and its evolution could provide useful insights into mitigating the detrimental impact of particle emissions.

Transmission Electron Microscopy (TEM) analysis of soot particles directly sampled from a diesel spray flame has emerged to be a powerful and quantitative technique for studying the soot particle size. This direct soot sampling technique has been successfully applied in reacting diesel jets, under high-pressure and high-temperature ambient conditions for soot study in a constant volume vessel [8, 9, 10, 11, 12, 13, 14], and in diesel engines [15, 16, 17]. Kook and Pickett [8] studied the morphology of soot particles extracted from diesel spray flames at ambient temperature and density of 1000 K and 6.7 MPa, respectively, in a constant volume vessel by using a thermophoretic probe. The TEM analysis of the soot samples along different in-flame axial locations revealed that the diameters of primary soot increase at first, reach a peak, and then decrease [8], in which the decrease in primary soot size is due to the soot oxidation process. Several studies [9, 18] showed a similar trend. A similar sampling technique and TEM analysis were used by Kuribayashi et al. [14] to study the effect of O_2 level (15% and 21%) on soot concentration, size, number density, and morphology in a diesel spray flame. They found that lowering the ambient O_2 concentration resulted in a delayed and downstream-shifted soot processes, as well as an increase in the aggregate size in the downstream region. However, the primary soot size remained relatively stable when the O_2 concentration decreased from 21% to 15%. Besides this work, the same approach (direct sampling and TEM analysis) has also been applied in other studies, such as fuel comparison among conventional diesel, biodiesel, and Fischer-Tropsch Diesel [11, 12], the effect of injected fuel amount [17], and nanostructure analysis of primary particles [19, 20]. Despite successful implementation in various studies, a major limitation of the direct soot sampling and TEM analysis is the time resolution. Since the thermophoretic probe is constantly exposed to the diesel flame, the sampled soot is a time-integrated mixture of soot particles throughout the injection and combustion duration. Therefore, the use of Computational Fluid Dynamics (CFD) is expected to overcome the limitations of TEM analysis of the sampled soot by providing the instantaneous spatial or temporal information of the soot formation processes.

There are a few methods to model the soot size distribution. One approach is the method of moments (MOM) [21], in which the evolution equations for moments of the population distribution are solved instead of explicitly solving the population distribution [22]. MOM was used by Ito et al. [23] who compared the predicted primary soot size from MOM against the measurement data from a laser-induced incandescence experiment of *n*-heptane spray combustion in a constant volume chamber. Recently, Naik et al. [24] utilized MOM in their simulation study of high-pressure lifted flames in a constant volume chamber. In addition to *n*-heptane fuel, a two-component surrogate fuel, conventional U.S. No. 2 diesel (D2), and world-averaged jet fuel (Jet-A) were considered in their simulation study [24]. Another approach is the discrete-sectional method (DSM) [25, 26, 27], which discretizes the population of soot particles into discrete sections or "bins," and the evolution equations are solved for each of these bins. This method has been applied to model primary soot size distribution in the optical engine [28, 29]. It is important to note that MOM only predicts the ensemble-averaged quantities where the exact shape of the particle size distribution is unknown. As for DSM, in order to achieve good accuracy, a higher number of sections are needed to represent the particle size distribution, thus making it computationally expensive. It is also noteworthy that both MOM and DSM can only provide the mean primary particle soot size and do not provide information about the history of the soot particles, which may contain vital information to understand the soot processes.

The Lagrangian tracking method is an alternative to DSM and MOM for computing particle dynamics. It allows the possibility to track an individual particle continuously along its trajectory and to monitor its individual interaction with the gas-phase and other particles. No classes or sections of particles are required, thus making the calculation of the particle size distribution relatively straightforward. Gallen et al. [30] introduced a semi-deterministic Lagrangian particle tracking methodology that tracks the Lagrangian soot particles, as well as considers their collision process. A hybrid Eulerian-Lagrangian method for soot modelling, which was developed by Dellinger et al. [31], combined a reduced gas-phase chemistry, a sectional model for polycyclic aromatic hydrocarbons (PAH), and a Lagrangian description of soot particles dynamics. The Lagrangian soot particles were nucleated from PAH molecules and radicals. Meanwhile, a two-way coupling of the gaseous and solid phases was assumed. It is important to note that the aforementioned studies were both related to gas turbine applications. A Lagrangian soot tracking (LST) model based on a semi-empirical formulation was recently developed by Ong et al. [32] and was successfully implemented for diesel spray applications. The LST model was validated against the experimental data of *n*-dodecane and *n*-heptane spray flame from the Engine Combustion Network (ECN). Despite omitting the coagulation process, the LST model was demonstrated to be able to predict primary soot

size, track individual soot particles, and access their history as the soot particles evolve in the diesel spray flame.

Setting against this background, the present study is carried out by coupling the previously developed LST model [32] with a reduced *n*-heptane chemical mechanism to investigate the effect of ambient O_2 and density on primary soot size in a Sandia *n*-heptane reacting spray. The article is structured such that the numerical formulation and setup are first provided. This is followed by the validation of CFD models using the non-reacting and reacting spray experimental data from ECN. The validation of the LST method is carried out by comparing the distribution of the steady-state soot volume fraction (SVF). Following this is the study of the soot size distribution for soot particles formed at the core of the jet during the transient and the steady-state phase.

2. Numerical Formulation and Setup

2.1. Mesh and Numerical Models

The computational study was performed using the spray combustion solver in an open-source code, OpenFOAM version 2.0.x [33]. Experimental data from the Sandia combustion vessel [34] was used for the model validation of the *n*-heptane spray and its combustion characteristics. Detailed descriptions of the experimental setup are available in [34]. The constant volume combustion vessels were represented by a cylinder during simulation studies. For computational expediency, the cylindrical chamber was simplified to a 4-degree axisymmetric wedge with a single layer of cells in the tangential direction. Details of the mesh and geometry can be found herein [32]. The time-step size was fixed at 0.2 μs. The non-reacting spray case was studied at an ambient temperature of 1000 K and ambient density of 14.8 kg/m^3 with the absence of oxygen (0% O_2 in ambient gas composition). As for the reacting spray case, there were a total of four cases with two O_2 concentrations (15% and 12%) and two ambient densities (14.8 kg/m^3 and 30 kg/m^3), while having the same initial ambient temperature of 1000 K. Cases with an ambient density of 14.8 kg/m^3 and 30 kg/m^3 were henceforth addressed as low density and high density cases, respectively, for brevity. Injection specifications and profiles in the current simulations were set to correspond to those used in the experimental setup. Details of the experimental conditions and the injection parameters are shown in Table 1.

The spray breakup was described using the Reitz-Diwakar model [35]. The model constant that governs the time factor for stripping, C_s, was set to 11.5. The turbulent flow was modeled using the Unsteady Reynolds-Averaged Navier-Stokes (URANS) method with the standard $k-\varepsilon$ model [36]. The model constant $C_{1\varepsilon}$ was calibrated according to its approximation of round jets [37, 38] and set to a value of 1.53. The initial turbulence kinetic energy k was set to 0.735 m^2/s^2, which was estimated based on the measured RMS velocity in the experiment [34]. The initial turbulence dissipation rate ε was set to 5.67 m^2/s^3 based on the turbulence integral length scale of 0.01 mm. The choice of the initial k and ε are similarly used in Refs. [38, 39, 40]. The average velocity in the combustion chamber prior to spray injection is approximately 0.7 m/s as provided in ECN [34]. This gas velocity is too low to cause a significant effect on the spray development as the spray velocity is 400-600 m/s. Therefore, the initial velocity field for all cases was set to be zero. A similar treatment of the initial velocity field can be seen in Ref. [39]. Soot radiation modeling was neglected in all test cases [41]. Collision and coalescence of the liquid spray were omitted in all studies as these processes have a negligible influence on the liquid and vapor fuel penetration of the evaporating spray [42]. In addition, the Ranz-Marshall correlation [43] was implemented to calculate the droplet heat transfer with the surrounding gas-phase, while the Frossling correlation [44] was used to model the evaporation of droplet fuel. The skeletal *n*-heptane mechanism developed by Pang et al. [45] was implemented to describe the chemical kinetics of *n*-heptane spray combustion. Details about the mechanism can be referred to in [45]. In this current study, the spray combustion solver was incorporated with an LST model [32]. The LST model is explained in detail in our previous study [32], but for completeness, the essential features are outlined here.

2.2. LST Model for Soot Particles

The LST model treats soot particles as Lagrangian particles, and the particles are tracked via the Lagrangian method, in

TABLE 1 Experimental conditions for Sandia *n*-heptane test cases. Data taken from Ref. [34].

Spray configuration	T_{am} [K]	ρ_{am} [kg/m^3]	O_2 [%]	Injection duration [ms]	Nozzle orifice diameter [mm]	Injection pressure drop [MPa]	Total fuel mass [mg]
Non-reacting	1000	14.8	0	6.8	0.1	150	17.8
Reacting	1000	14.8	15	6.8	0.1	150	17.8
			12	6.8	0.1	150	17.8
	1000	30.0	15	6.8	0.1	150	18.0
			12	6.8	0.1	150	17.8

T_{am}: ambient temperature; ρ_{am}: ambient density; O_2 %: ambient oxygen concentration (in mole fraction).

which the motion of the soot particles is computed using Newton's second law of motion. The dispersion of Lagrangian particles due to turbulence is influenced by the instantaneous fluctuating velocity $\vec{u'}$ [46, 47], which is modeled by the discrete random walk model [46, 47]. It correlates with the flow turbulent kinetic energy k predicted by the standard $k-\varepsilon$ model and is expressed by

$$\vec{u'} = \zeta \sqrt{2k/3} \begin{Bmatrix} 1 \\ 1 \\ 1 \end{Bmatrix} \quad \text{Eq. (1)}$$

where ζ is a Gaussian random number [45, 46] with zero mean and unit variance.

The LST model also considers the inception, surface growth, and oxidation processes of the soot particles. It is important to note that the coagulation process is omitted in the LST model as the soot surface growth is the relatively dominant process in affecting the primary soot particle size [48, 49]. The inception, surface growth, and oxidation rates in the LST model are adapted from the semi-empirical, multi-step Moss-Brookes (MB) soot model [50]. The MB soot model is chosen due to its flexibility in implementing different surface aging models, as shown in Ref. [51].

The inception rate ω_{inc} is given by

$$\omega_{inc} = C_{inc} M_P \left(\frac{X_{prec} P}{RT} \right) \exp\left\{ -\frac{T_{inc}}{T} \right\} \quad \text{Eq. (2)}$$

where X_{prec} denotes the mole fraction of the soot precursor, whereas C_{inc} is the model constant for soot incipient rate and is given as 54 s^{-1}. T, P, and R denote the gas temperature, pressure, and universal gas constant, respectively. The activation temperature of soot inception T_{inc} is given as 21,000 K. The constant M_P represents the mass of an incipient soot particle, which is set to 1200 kg/kmol. In the LST model, Lagrangian particles are formed when a formation criterion in a computational cell is met. The formation criterion at cell j is given as

$$m_{inc,j} > m_{inc,min} \quad \text{Eq. (3)}$$

where $m_{inc,j}$ denotes the total incipient soot mass at cell j and $m_{inc,min}$ denotes the minimum mass of incipient soot. $m_{inc,j}$ is calculated by taking the product of $\omega_{inc,j}$ and the time step Δt. Meanwhile, $m_{inc,min}$ is calculated to be 2.0×10^{-24} kg, based on the assumption that the minimum diameter of incipient soot is 1.24 nm [52], with the soot density of 2000 kg/m^3 [52, 53]. The single formed Lagrangian particle is assumed to represent the total number of incipient soot particles in that particular computational cell at that time instance. It is also assumed that all particles formed in that cell, at that instant, follow the same pathway [54] and size change as the existing Lagrangian particle. The initial velocity of the new particle formed follows the mean velocity of the cell it is formed in.

The newly formed Lagrangian particles then undergo mass addition and increase in size through the surface growth process and decrease in size due to oxidation processes via hydroxyl radicals (OH) and O_2. The rate of change of the soot diameter due to surface growth is governed by Equation 4, whereas the diameter change due to oxidation is given by Equations 5 and 6.

$$\left.\frac{d}{dt}(d_i)\right|_{SG} = \alpha \left[2C_{sg} \left(\frac{X_{sg} P}{RT} \right) \frac{1}{\rho_{soot}} \exp\left\{ -\frac{T_\gamma}{T} \right\} \right] \quad \text{Eq. (4)}$$

$$\left.\frac{d}{dt}(d_i)\right|_{ox\,via\,OH} = 2C_{OH}\, \eta_{coll} \left(\frac{X_{OH} P}{RT} \right) \frac{\sqrt{T}}{\rho_{soot}} \quad \text{Eq. (5)}$$

$$\left.\frac{d}{dt}(d_i)\right|_{ox\,via\,O_2} = 2C_{O_2} \left(\frac{X_{O_2} P}{RT} \right) \frac{\sqrt{T}}{\rho_{soot}} \exp\left\{ -\frac{T_{O_2}}{T} \right\} \quad \text{Eq. (6)}$$

The mole fraction for the surface growth species is denoted as X_{sg}. The mole fractions for soot oxidants, OH and O_2, are represented by X_{OH} and X_{O_2}, respectively. It is important to note that acetylene is chosen here as the surface growth species and soot precursor species. Although PAH is also an important soot precursor. To accurately predict the formation of PAH, a larger chemical mechanism that includes PAH formation pathways is required, which will incur a higher computational cost. Furthermore, there are numerous numerical studies of soot formation in diesel spray flame that consider only acetylene as their soot precursor, e.g., Refs. [38, 55-57]. Therefore, only acetylene is chosen in this study as the soot precursor to achieve a balance between accuracy and computational efficiency. Furthermore, a one-way coupling is assumed between the Lagrangian soot particles and the gaseous species. This implies that the gaseous species affects the Lagrangian soot particles, but not the other way around. The soot model constants, their descriptions, and values are shown in Table 2. The α in Equation 4 denotes the surface aging factor, which is assumed to be a function of temperature and is expressed as

$$\alpha = \frac{1}{2} \left(\tanh\left(\frac{8168}{T} - 4.57 \right) + 1 \right) \quad \text{Eq. (7)}$$

TABLE 2 The soot model constants. Data taken from Refs. [50, 52].

Soot model constants	Descriptions	Value [unit]
C_{sg}	Surface growth rate scaling factor	11,700 [kg m $kmol^{-1}$ s^{-1}]
C_{OH}	Model constant for soot oxidation due to OH	105.81 [kg m $kmol^{-1}$ $K^{-0.5}$ s^{-1}]
C_{O_2}	Model constant for soot oxidation due to O_2	8903.51 [kg m $kmol^{-1}$ $K^{-0.5}$ s^{-1}]
T_{sg}	Activation temperature of surface growth	12,100 [K]
T_{O_2}	Activation temperature of soot oxidation due to O_2	19,778 [K]
η_{coll}	Collision efficiency parameter	0.13 [—]

Once a Lagrangian soot particle is reduced below a threshold diameter, it is assumed to be fully oxidized and is removed from the computational cell. The threshold value is set to 1.24 nm, which is the same as the initial incipient soot particle size.

3. Results and Discussion

3.1. Validation of Numerical Models

The first part of this section compares the simulation results of the non-reacting fuel spray against experimental measurements, in terms of liquid (LPL) and vapor penetration (LPL) lengths as well as radial profiles of the mixture fraction. This is followed by the validation of the computed ignition delay times (IDT) and lift-off lengths (LOL) of the reacting spray to the experimental data [34]. The non-reacting and reacting spray validation cases are carried out to ensure that the fuel-air distribution and combustion characteristics are reasonably simulated, and the uncertainties induced by these elements can be minimized prior to studying the soot formation events. The validation of the LST model is carried out by comparing the predicted SVF profiles with measured data during steady-state combustion under different ambient conditions.

In the current work, the LPL is taken as the axial location from the injector to the location where 99% of the total liquid mass is found, while the VPL is taken as the maximum distance from the nozzle outlet to where the fuel mass fraction (or mixture fraction) is 0.1%. As for the LOL, it is defined as the first axial location of the Favre-averaged OH mass fraction, which reaches 2% of its maximum value in the domain. The time-averaging of the simulated LOL is carried out from 3.0 ms to 6.0 ms. This corresponds to the experimental definition. The IDT is defined as the time when the greatest rise of maximum temperature is observed, $\left(\frac{dT_{max}}{dt}\right)_{max}$, and this definition remains consistent throughout the study. Although there are other definitions for the IDT, it is shown that there is no significant discrepancy in the IDT between different IDT definitions [39]. Moreover, this definition is in accordance with the recommendation by the ECN [34].

3.1.1. Non-reacting Spray Simulations Comparisons between the computed and measured penetration lengths are depicted in Figure 1(a) using the default and calibrated model constant. In general, the tuned model shows an improved VPL and LPL prediction as compared to the measurement. Computed and measured mean radial mixture fraction profiles are next compared in Figure 1(b). The overall trend of the mixture fraction profiles agrees with the experimental data, which implies that the fuel-air distributions are reasonably predicted by the model.

3.1.2. Reacting Spray Simulations Figure 2 shows the comparison of the experimental and predicted IDT/LOL

FIGURE 1 (a) Comparison of liquid and vapor penetration length for the non-reacting *n*-heptane spray case. (b) Comparison of the simulated and experimental radial mixture fraction of the non-reacting *n*-heptane spray case at different axial locations and time after injection.

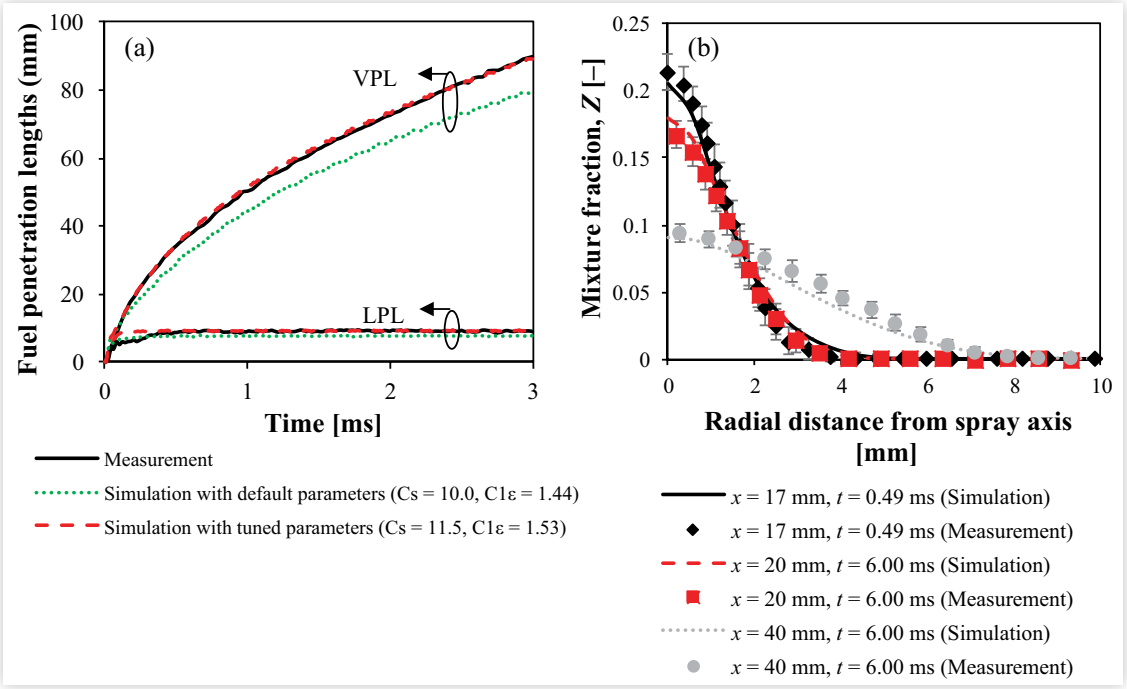

FIGURE 2 Comparison of the simulated ignition delay time and lift-off length for the reacting *n*-heptane spray cases with experimental results at different ambient oxygen levels and ambient densities. (Hollow symbols represent measured data; Filled symbols represent simulation data.)

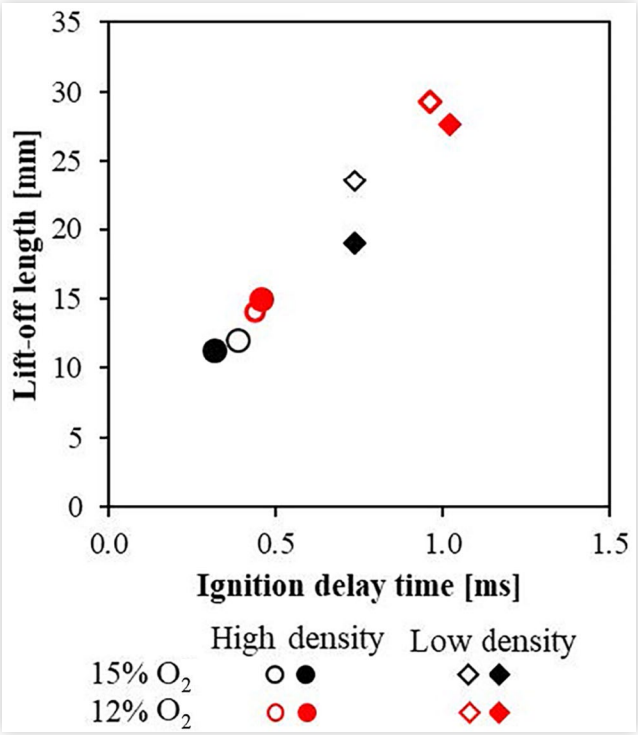

for the reacting *n*-heptane spray cases at different O_2 levels and ambient densities. At a low density, the predicted IDTs correspond well with the measured IDT for 15% and 12% O_2 levels with a maximum relative difference of 7.3%. A maximum relative difference of 17.5% is obtained for the predicted IDT at a higher ambient density of 30.0 kg/m^3. At a high density condition (30.0 kg/m^3), the predicted LOLs at both O_2 levels are within a relative difference of 7% as compared to the experimental LOL. At a low density condition (14.8 kg/m^3), the predicted LOL at 12% O_2 and 15% O_2 are underpredicted by 6% and 20%, respectively. Nevertheless, the simulated LOLs are shown to correspond well with the measured data for all the reacting spray cases by capturing the LOL trend, where the LOL increases with increasing ambient density and decreasing O_2 levels.

3.1.3. Steady-State SVF Distribution In this section, the predicted SVF results using the LST model are compared against the measured SVF for different O_2 levels and ambient densities. The experimental SVF is obtained from the time-averaged line-of-sight extinction (KL) data [34]. Predicted SVF using the LST model is calculated based on the total number of Lagrangian soot particles in the domain. Figure 3 shows the temporal evolution of the number of Lagrangian soot particles under different ambient densities and O_2 levels. It is depicted in the figure that the number of soot particles reaches a quasi-steady state at $t \geq 4$ ms. Therefore, the predicted steady-state SVF using the LST model is obtained by time-averaging the computed SVF from 4 ms to 6 ms. In addition, normalization is carried out by normalizing the simulated and measured SVF with their respective peak SVF at 15% O_2 and 30.0 kg/m^3 density. The normalized SVF profiles for different O_2 levels and ambient densities along the spray axis are shown in Figure 4. The simulated SVF for the 12% O_2, 30.0 kg/m^3 density case is underpredicted by approximately 30% relative to the measured data. At the low density condition, the predicted SVF at 15% O_2 is overpredicted by a factor of two as compared to the measured result. The larger discrepancy at 15% O_2 is likely due to the underpredicted LOL, which leads to less air entrainment into the spray and subsequently higher soot formation (cf. Figure 2). Despite these discrepancies, the predicted SVF using the LST model is shown to increase with increasing O_2 level and ambient density, which corresponds with the experimental observation as depicted in Figure 4. The spatial location of the predicted SVF is further downstream than the measured SVF. This can be attributed to the use of the Moss-Brookes soot model in the formulation of the LST model, which is discussed in [32]. It is shown in Ref. [39] that considering the surface-aging effect in the surface growth model can cause the spatial location of the soot cloud to be more upstream. Therefore, it is expected that implementing a more advanced surface-aging model than the one implemented in the present study will likely improve the spatial prediction of the LST model. Despite the overprediction, the LST model is able to capture the variation of the spatial location of SVF towards the upstream location of the spray as O_2 level increases and ambient density increases, which coincide with the experimental observation (cf. Figure 4). It is important to note that a single simulation case using the LST model requires approximately 170 hours to reach 6.0 ms after start of fuel injection when running in serial on an HP Z200 Workstation with Quad-Core Intel Xeon Processor 3400 at 2.40 GHz.

3.2. In the Spray Core Jet

3.2.1. Sampling of Individual Lagrangian Soot Particles The soot sampling experiment was conducted by Aizawa and colleagues, in which full details of the experimental methodology can be seen in Refs. [11-13]. For completeness of the present article, only the essential steps are highlighted here. The soot sampling experiment involves placing a probe in parallel to the spray axis to skim the gas containing soot from the spray flame while minimizing the flow disturbance to the other half of the spray flame. As the reacting flow passes the probe, soot particles are deposited onto the carbon-coated copper grid inside the probe via thermophoresis. The sampled soot particles correspond to the soot present at that position. Sampled soot particles at different locations along the spray axis can be obtained by repeating the experiment with the probe being at different locations along the spray

FIGURE 3 Temporal evolution of the number of computational particles for soot under different ambient densities and oxygen levels.

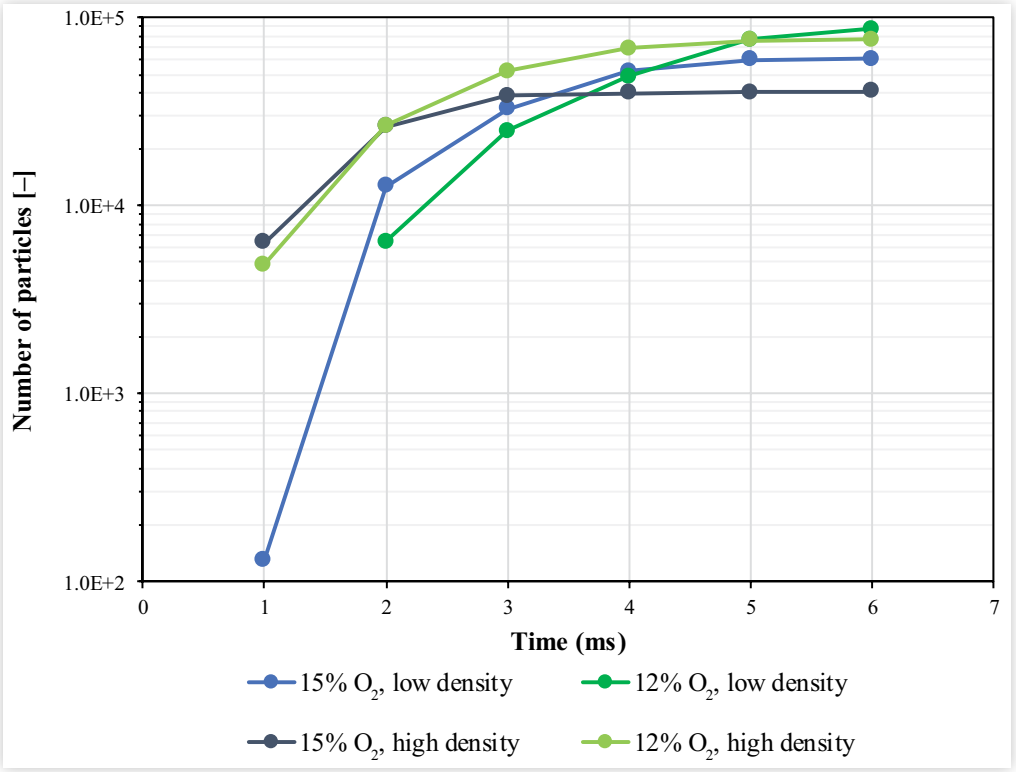

FIGURE 4 Normalized SVF as a function of the axial distance from the injector at oxygen levels of 15% and 12% with ambient densities of 14.8 kg/m^3 (low density) and 30.0 kg/m^3 (high density).

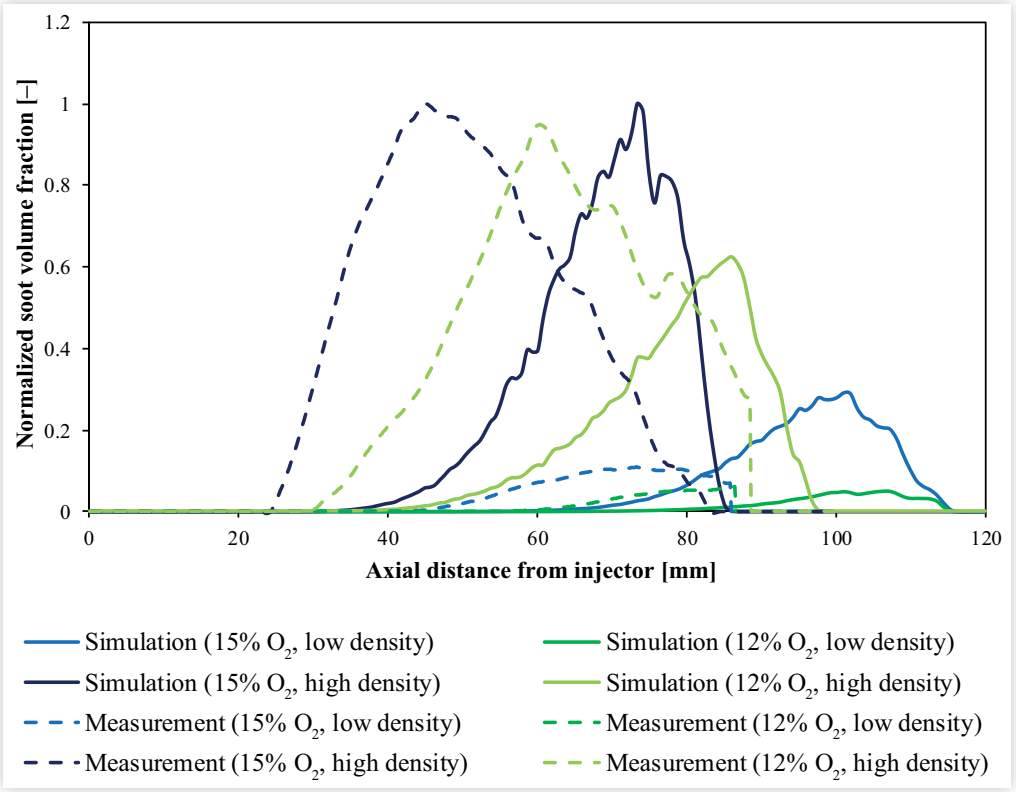

axis. The sampled soot particles are then observed under a High-Resolution Transmission Electron Microscope. The diameter of each primary soot particle is finally obtained by manually processing the TEM images.

To replicate the same sampling technique along the spray axis in our CFD studies, Lagrangian particles, which are ±1.5 mm axially and ±0.5 mm radially about the sampling locations, are assumed to be deposited onto the sampler, and thus, their information is recorded. A similar analysis was carried out in our previous work [32]. Information of the deposited Lagrangian particles, such as size, position, velocity, etc., are gathered from the start of ignition (SOI) to 6.0 ms after start of ignition (ASOI). The analysis of the information gathered for the individual Lagrangian particles is later carried out in subsequent sections to obtain the primary soot size distribution and study its relation to soot processes.

3.2.2. Primary Soot Size Distribution The effect of ambient O_2 and density on primary soot size distribution at the core of the spray jet for the *n*-heptane spray cases are investigated here. The probability density function (PDF) of primary soot size for various ambient O_2 levels and ambient densities cases are shown in Figure 5. It is observed that the onset location of soot moves downstream as the O_2 level decreases. Soot is present at x = 50 mm for the 15% O_2, low density case, while soot is only present further downstream at x = 60 mm for the 12% O_2, low density case. This phenomenon is similarly captured in the high-density case (not shown in the figure).

FIGURE 5 Probability density function of the primary soot size predicted along various axial locations from the injector location for different ambient oxygen level and density cases.

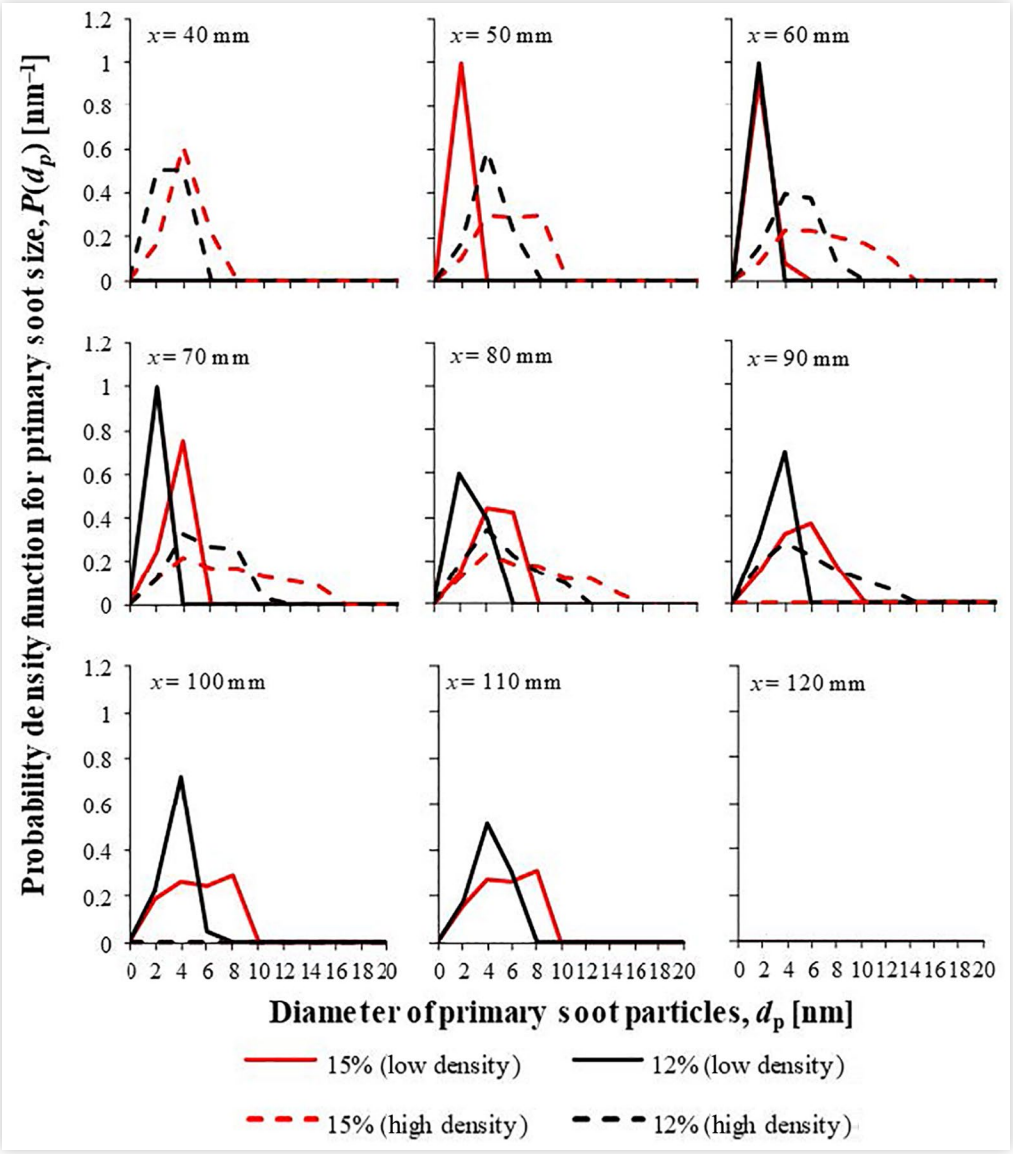

The variation of soot onset location with the O_2 level coincides with the experimental observation in [58, 59, 60] and in Section 3.1.3. Furthermore, Figure 5 also shows that, in all the cases, the primary soot diameters increase as soot particles migrate downstream. This is caused by the soot undergoing surface growth process and is consistent with experimental observations [8, 9, 18].

The mean primary soot diameter is computed from the collected Lagrangian particles along the core of the spray jet from the SOI to 6.0 ms ASOI and is shown in Figure 6. The mean primary soot size predicted at the O_2 level of 15% and ambient density of 30 kg/m^3 is in reasonable agreement with the measured mean primary soot size using *n*-dodecane fuel [61]. In the low density case, the mean primary soot size reaches a peak value of approximately 4.5 nm and 3.2 nm for O_2 levels of 15% and 12%, respectively. As the ambient density increases to 30.0 kg/m^3, the peak value of the predicted mean primary soot size increases to 6.2 nm and 4.5 nm for oxygen levels of 15% and 12%, respectively. This implies that an increase in the ambient density resulted in the primary soot size to increase by a factor of 1.5. Furthermore, it is also evidently shown in Figure 6 that the mean primary soot size decreases with decreasing O_2 levels. There have been no experimental studies on the effect of ambient O_2 and density on primary soot size in diesel spray flame for *n*-heptane fuel. However, experimental studies on SVF have shown that decreasing ambient O_2 [58] and increasing ambient density [62] can increase the SVF in the diesel spray flame. In addition, measurement of the primary soot size in canonical flame setups also showed similar findings regarding the effect of O_2 [63] and ambient density [64, 65, 66] on primary soot sizes.

The results presented in Figures 5 and 6 are time-integrated results of all the collected Lagrangian particles along the core of the spray jet from the SOI to 6.0 ms ASOI. To gain a better insight into the effect of ambient O_2 and density on the primary soot size, the instantaneous primary soot size and the corresponding net growth rates experienced by the soot particles are analyzed next. The temporal evolution of the net growth rates in all the cases is presented in Figure 7. Moreover, their corresponding evolution of the primary soot size distribution with respect to the axial distance is presented in Figure 8.

At low density (14.8 kg/m^3), the maximum net growth rates in the 15% O_2 and 12% O_2 cases are 1×10^5 kg/m^3/s and 0.25×10^5 kg/m^3/s, respectively. The span of the soot cloud in the 12% O_2 case is shorter than the 15% O_2 case from 1.0 ms ASOI to the steady-state period, as depicted in Figures 7(a)-(d). The evolution of the primary soot size is shown in Figure 8 to correspond to the net growth rates for the 15% O_2 and 12% O_2 cases, where a larger soot size is achieved in the former case due to having higher net growth rates.

At high density, the net growth rates for the 15% O_2 case are higher than the 12% O_2 case (cf. Figure 7). Contrary to that in the low density case, the span of the soot cloud at both O_2 levels is comparable to one another during the early ignition stage ($t \leq$ 2 ms ASOI). However, the span of the soot cloud in the 12% O_2 case becomes longer than that in the 15% O_2 case at later times ($t \geq 3$ ms ASOI). During the steady-state period, the span of the soot cloud for the 12% O_2 case is 10 mm longer than that in the 15% O_2 case. The evolution of the primary soot size at high density condition shows a similar trend to the ones at the low density condition, where the primary soot size is larger for the 15% O_2

FIGURE 6 Mean primary soot size as a function of axial distance from the injector for different ambient oxygen level and density cases. The filled symbols refer to low density cases; hollow symbols refer to high density cases.

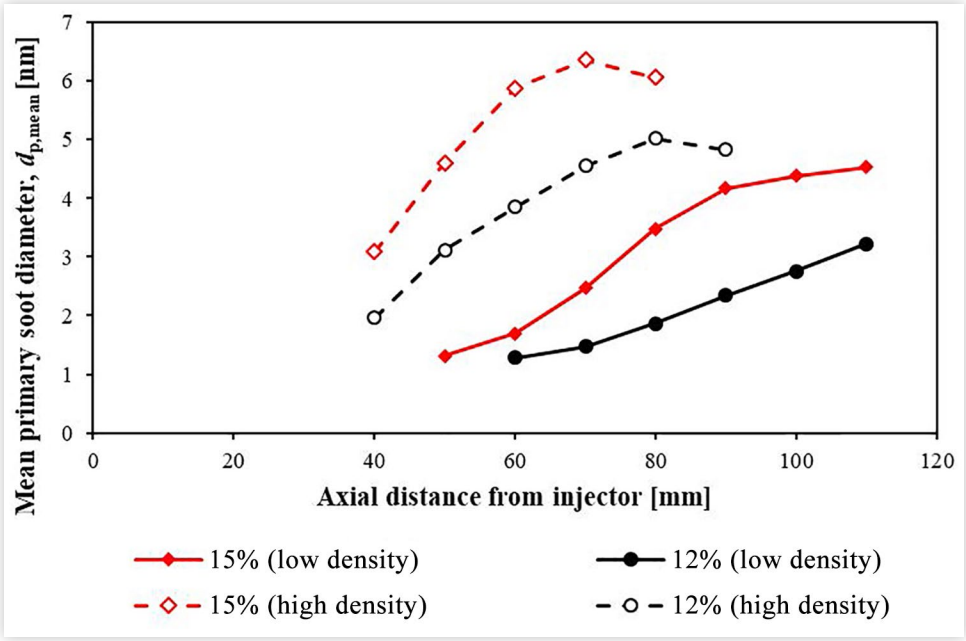

FIGURE 7 Temporal evolution of the net growth rates at the core of the spray jet for different ambient oxygen levels and density cases at different timings. The filled symbols refer to low density cases; hollow symbols refer to high density cases.

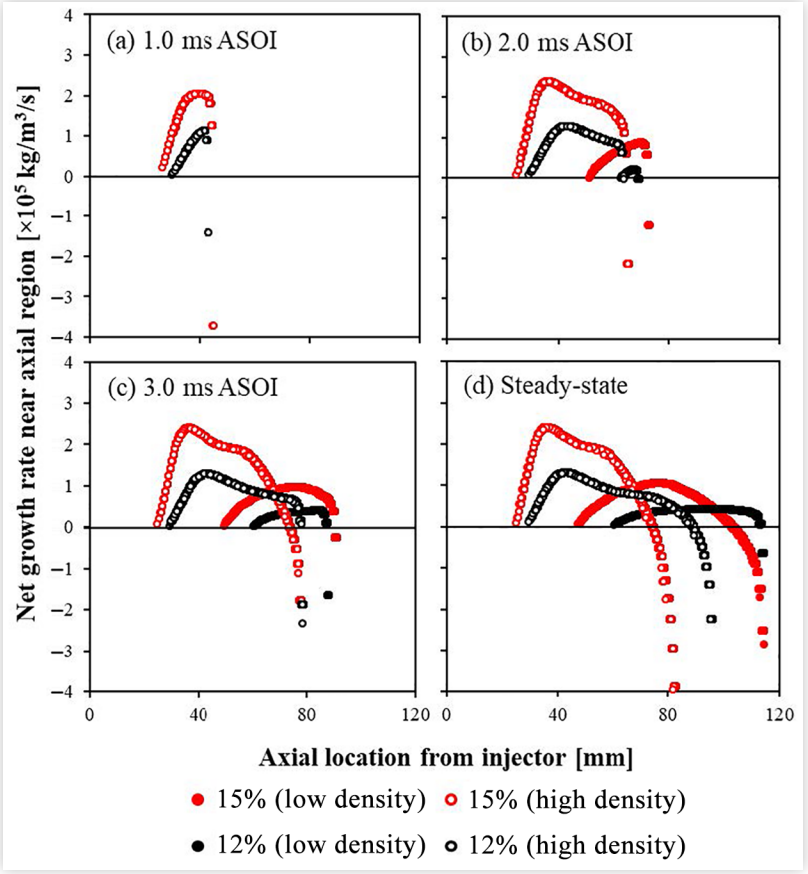

(cf. Figure 8). In addition, increasing the ambient density while keeping the ambient O_2 constant leads to an increase in primary soot sizes. This is likely due to the higher net growth rate achieved at higher ambient density condition, as depicted in Figure 7.

3.2.3. Soot Age Distribution As the previous section has clearly demonstrated that the soot cloud span varies with different ambient conditions, it is expected that the longer span of the soot cloud would imply a longer soot residence time in the spray flame. The use of the LST model allows the ability to analyze the residence time of soot in the spray flame by tracking the soot particles from the time of formation to the time of oxidation. The time duration of the soot particle from formation till oxidation is henceforth known as soot age [67]. It is important to note that the transient analysis of soot age is carried out after soot onset (ASO), where the soot onset time and soot onset location are tabulated in Table 3. The soot onset time is defined here as the earliest time after SOI when the total number of Lagrangian soot particles present in the domain are more than 100 particles. The soot onset location is taken as the axial distance from the nozzle to the point where the maximal SVF is present at the soot onset time. From Table 3, it is shown that the soot onset time and location increase as the O_2 level decreases at both ambient densities. Shorter soot onset time and a more upstream soot onset location are obtained when the ambient density increases. These results agree qualitatively with the experimental and numerical findings in [59], which uses *n*-dodecane as fuel.

Figure 9 shows the predicted temporal evolution of the soot age distribution of the primary soot particles at the core of the spray jet with different ambient O_2 levels and densities. From 1.0 ms to 3.0 ms ASO, the soot age distributions at different O_2 levels and ambient densities are similar to one another. A narrower distribution is obtained in the 15% O_2 case at high density as compared to the other cases at 4.0 ms ASO, which implies that the soot particles in the 15% O_2, high density case have a relatively shorter soot age than the other cases.

It is mentioned in Section 3.2.2 that the soot cloud span for the 12% O_2, low density case is shorter than the 15% O_2, low density case before reaching the steady-state period.

FIGURE 8 Primary soot size distribution at the core of the spray jet for different ambient oxygen level and density cases. (a)–(d) refer to low density cases and (e)–(f) refer to high density cases.

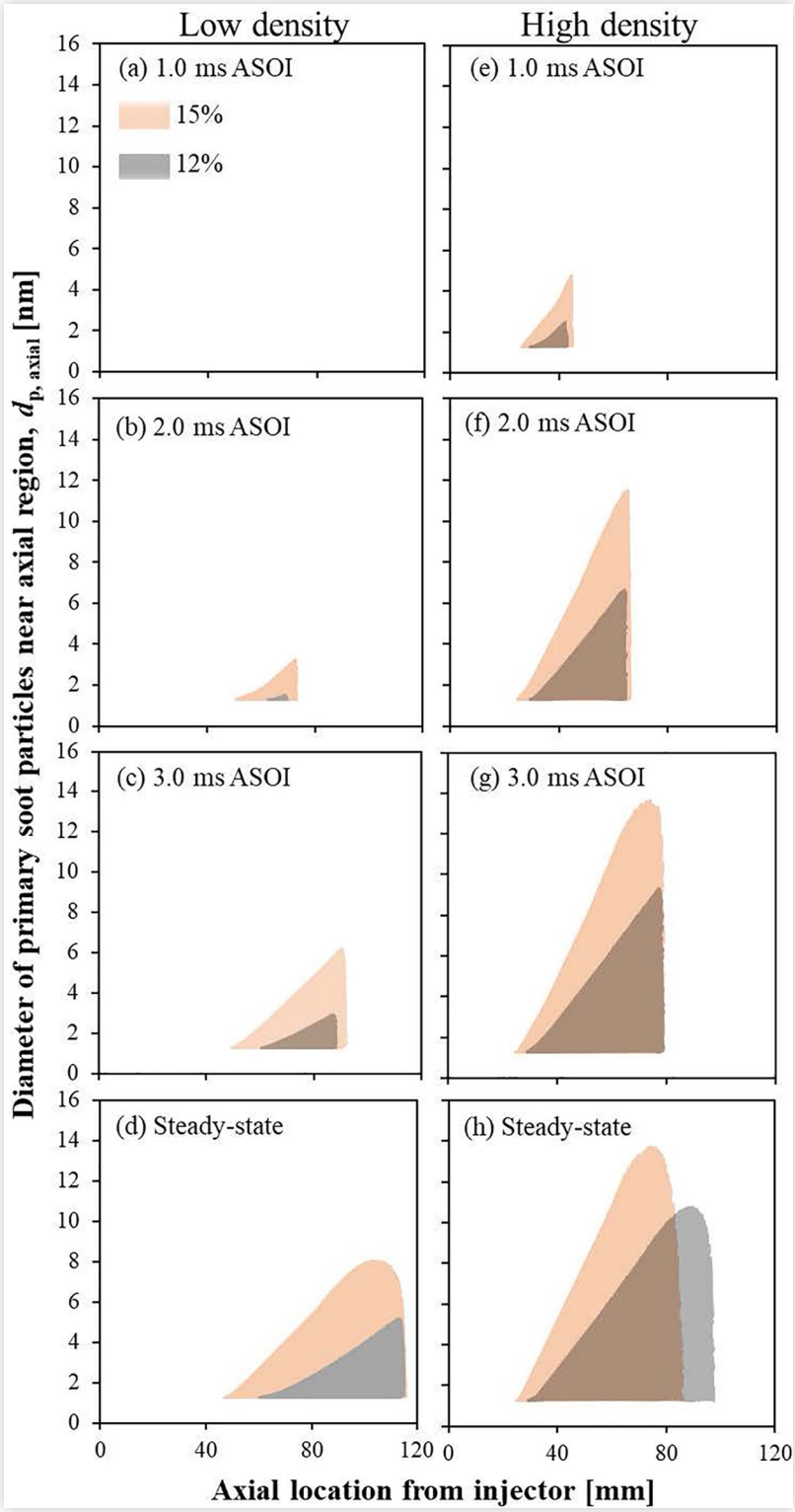

TABLE 3 Soot onset time and onset location for different ambient oxygen levels and densities of *n*-heptane spray cases.

Ambient density [kg/m^3]	Ambient oxygen [%]	Soot onset time [ms]	Soot onset location [mm]
14.8	15	0.94	48
	12	1.38	58
30.0	15	0.41	27
	12	0.57	30

Despite having a shorter soot cloud span, the soot age distribution in Figure 9 shows no significant difference between both O_2 level cases. This can be explained by the difference in the soot onset location in both cases. As mentioned earlier, the soot onset location for the 15% O_2, low density case is more upstream than the 12% O_2 case (as shown in Table 3). As the soot particles are formed nearer to the nozzle, the flow velocity experienced by the soot particles is higher than the ones further downstream. Therefore, the time taken to travel along the spray flame is shorter. Meanwhile, the soot onset location for the 12% O_2 case is further downstream. The lower flow velocity experienced by the soot particles consequently leads to particles traveling more slowly through the spray flame.

In the high density case, the 15% O_2 case has a much narrower soot age distribution at 4.0 ms ASO [cf. Figure 9(d)] and a shorter soot cloud span than that in the 12% O_2 case during the steady-state period [cf. Figure 8(h)]. This observation can also be attributed to the soot onset location. The soot onset location for both O_2 levels is close to one another, as shown in Table 3. This implies that the flow velocities experienced by the soot particles at both O_2 levels are not significantly different. Therefore, the shorter soot cloud span in the 15% O_2 case would yield a shorter soot age as predicted in Figure 9(d). The results above also show that a longer soot cloud span does not necessarily equate to longer soot residence time. The residence time of the soot particles in a spray flame is dependent on both the soot cloud span and the soot onset location.

FIGURE 9 Soot age distribution of soot particles at the core of the spray jet for different ambient oxygen levels and densities at different timing ASO. Solid lines refer to low density cases; dashed lines refer to high density cases.

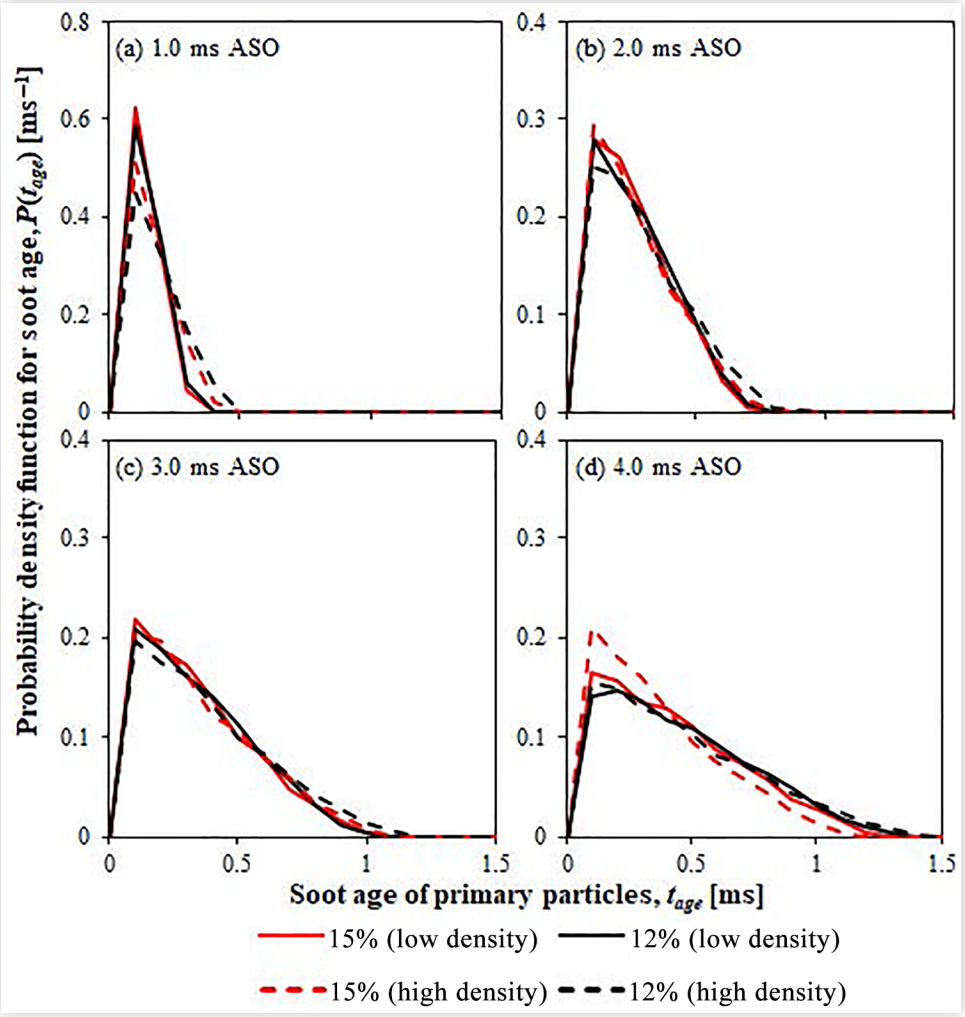

4. Conclusion

The effect of ambient O_2 level and density on the prediction of soot volume fraction (SVF) and soot size distribution is carried out using a Lagrangian Soot Tracking (LST) method on Sandia *n*-heptane spray cases. The simulated SVF for the 12% O_2, 30.0 kg/m^3 density case is underpredicted by approximately 30% relative to the measured data. At low density condition, the predicted SVF at 15% O_2 is overpredicted by a factor of two. Despite these discrepancies, the qualitative trend of the measured SVF where the SVF increases with the increasing O_2 level and ambient density is captured by the simulated SVF.

The peak primary soot size achieved in the core of the spray jet at an ambient density of 14.8 kg/m^3 and O_2 levels of 15% and 12% are 14 nm and 10 nm, respectively. Based on the primary soot size distribution in the core of the spray jet, an increase in ambient density from 14.8 kg/m^3 to 30 kg/m^3 is shown to increase the peak and mean primary soot size by a factor of 1.5. Furthermore, the peak and mean primary soot size decrease with decreasing O_2 levels from 15% to 12%. A higher O_2 level and ambient density lead to a higher net growth rate experienced by the soot particles, resulting in larger primary soot sizes. At low density condition, the soot cloud span is shorter in the 12% O_2 case as compared to that in the 15% O_2 case. On the contrary, the high density cases show comparable soot cloud span for both O_2 levels before the steady-state period. With the introduction of the soot age, the present study shows that a longer span of the soot cloud does not equate to a longer soot residence time in the spray flame.

Despite having different soot cloud spans, the soot age distributions at different O_2 levels and ambient densities are similar to one another from 1.0 ms to 4.0 ms after soot onset time. The reason for this is likely due to the soot onset location. Soot particles that form upstream of the spray will experience a higher flow velocity, thus leading to a shorter soot age when the span of the soot cloud is short.

Acknowledgements

This research was conducted under the generous financial support from the University of Nottingham Malaysia Campus, by providing the Dean's Scholarship. JHW wishes to acknowledge support from the Independent Research Fund Denmark under the grant number 8022-00143B.

References

1. Chen, L., Liang, Z., Zhang, X., and Shuai, S., "Characterizing Particulate Matter Emissions from GDI and PFI Vehicles under Transient and Cold Start Conditions," *Fuel* 189:131-140, 2017.
2. Liu, H., Ma, X., Li, B., Chen, L. et al., "Combustion and Emission Characteristics of a Direct Injection Diesel Engine Fueled with Biodiesel and PODE/Biodiesel Fuel Blends," *Fuel* 209:62-68, 2017.
3. Kazemimanesh, M., Moallemi, A., Olfert, J.S., and Kostiuk, L.W., "Probe Sampling to Map and Characterize Nanoparticles along the Axis of a Laminar Methane Jet Diffusion Flame," *Proc Combust Inst* 36:881-888, 2017.
4. Bockhorn, H., "Combustion Generated Fine Carbonaceous Particles," in *Proceedings of an International Workshop*, Villa Orlandi, Anacapri, May 13-16, 2007 (KIT Scientific Publishing, 2009).
5. Schwartz, J., "Air Pollution and Daily Mortality: A Review and Meta Analysis," *Environ Res* 64:36-52, 1994.
6. European Parliament, Council of the European Union, REGULATION (EC) No. 715/2007 OF THE EUROPEAN PARLIAMENT AND OF THE COUNCIL of 20 June 2007 on type approval of motor vehicles with respect to emissions from light passenger and commercial vehicles (Euro 5 and Euro 6) and on access to vehicle repair and mai," Off J Eur Union 2007; L171:1-16, OJEU 29.6.2007 L171.
7. Le Coq, L., "Élimination Des Particules," *Tech l'Ingénieur* 33:20, 2006.
8. Kook, S. and Pickett, L.M., "Soot Volume Fraction and Morphology of Conventional and Surrogate Jet Fuel Sprays at 1000-K and 6.7-MPa Ambient Conditions," *Proc Combust Inst* 33:2911-2918, 2011.
9. Yamaguchi, T., Kondo, K., Nishigai, H., Takano, S. et al., "Direct Sampling, TEM Analysis and Optical Measurement of Soot Particles at Different Axial Locations in a Transient Spray Flame," *SAE Int. J. Fuels Lubr.* 5(1):316-328, 2011, https://doi.org/10.4271/2011-01-2051.
10. Kondo, K., Yamaguchi, T., Nishigai, H., Takano, S. et al., "High-Resolution Transmission Electron Microscopy of Soot Directly Sampled at Different Axial Locations in Diesel Spray Flame," SAE Technical Paper 2011-24-0068, 2011, https://doi.org/10.4271/2011-24-0068.
11. Aizawa, T., Nishigai, H., Kondo, K., Yamaguchi, T. et al., "Transmission Electron Microscopy of Soot Particles Directly Sampled in Diesel Spray Flame - A Comparison between US#2 and Biodiesel Soot," *SAE Int. J. Fuels Lubr.* 5(2):665-673, 2012, https://doi.org/10.4271/2012-01-0695.
12. Aizawa, T., Takahata, N., Okabe, K., and Mizutani, Y., "Effect of Fuel Aromatics on In-Flame Diesel Soot Nanostructure via HRTEM," SAE Technical Paper 2015-01-1829, 2015, https://doi.org/10.4271/2015-01-1829.
13. Kuribayashi, M., Ishizuka, Y., and Aizawa, T., "Sizing of Soot Particles in Diesel Spray Flame - A Qualitative Comparison between TEM Analysis and LII/Scattering Laser Measurements," *SAE Int. J. Fuels Lubr.* 6(3):641-650, 2013, https://doi.org/10.4271/2013-01-2576.
14. Kuribayashi, M., Mizutani, Y., Ishizuka, Y., Taki, N. et al., "Effects of Ambient Oxygen Concentration on Soot Processes in Diesel Spray Flame - A Qualitative Comparison between TEM Analysis and LII/Scattering Laser Measurements," *SAE Int. J. Fuels Lubr.* 7:693-703, 2014, https://doi.org/10.4271/2014-01-2642.
15. Kook, S., Zhang, R., Szeto, K., Pickett, L.M. et al., "In-Flame Soot Sampling and Particle Analysis in a Diesel Engine," *SAE Int. J. Fuels Lubr.* 6(1):80-97, 2013, https://doi.org/10.4271/2013-01-0912.

16. Zhang, R. and Kook, S., "Structural Evolution of Soot Particles during Diesel Combustion in a Single-Cylinder Light-Duty Engine," *Combust Flame* 162:2720-2728, 2015.
17. Wang, Y., Liu, H., Li, T., Jiang, H. et al., "Characterization of the Morphology and Nanostructure of the Soot Particles Produced within Transient Diesel Reacting Jet Flame by Using Thermophoretic Sampling Technique," *Energy & Fuels* 33:9124-9137, 2019.
18. Nerva, J.G., Yamaguchi, T., Iguma, H., Nishigai, H. et al., "Transmission Electron Microscopy of Soot Particles Sampled Directly from a Biodiesel Spray Flame," SAE Technical Paper 2011-01-2046, 2011, https://doi.org/10.4271/2011-01-2046.
19. Sakai, M., Iguma, H., Kondo, K., and Aizawa, T., "Nanostructure Analysis of Primary Soot Particles Directly Sampled in Diesel Spray Flame via HRTEM," SAE Technical Paper 2012-01-1722, 2012, https://doi.org/10.4271/2012-01-1722.
20. Jiang, H., Li, T., Wang, Y., He, P. et al., "The Evolution of Soot Morphology and Nanostructure along Axial Direction in Diesel Spray Jet Flames," *Combust Flame* 199:204-212, 2019.
21. Frenklach, M., "Method of Moments with Interpolative Closure," *Chem Eng Sci* 57:2229-2239, 2002.
22. Mueller, M.E., Blanquart, G., and Pitsch, H., "A Joint Volume-Surface Model of Soot Aggregation with the Method of Moments," *Proc Combust Inst* 32:785-792, 2009.
23. Ito, T., Hosaka, T., Ueda, M., Senda, J. et al., "Detailed Kinetic Modeling and Laser Diagnostics of Soot Formation Process in Diesel Jet Flame," *SAE Trans.* 113(4):602-613, 2004, https://doi.org/10.4271/2004-01-1398.
24. Naik, C.V., Puduppakkam, K.V., and Meeks, E., "Simulation of Soot Volume Fraction and Size in High-Pressure Lifted Flames Using Detailed Reaction Mechanisms," in *ASME Turbo Expo 2014 Turbine Tech Conf Expo*, Düsseldorf, Germany, 2014, V04BT04A025.
25. Gelbard, F. and Seinfeld, J.H., "Simulation of Multicomponent Aerosol Dynamics," *J Colloid Interface Sci* 78:485-501, 1980.
26. Gelbard, F., Tambour, Y., and Seinfeld, J.H., "Sectional Representations for Simulating Aerosol Dynamics," *J Colloid Interface Sci* 76:541-556, 1980.
27. Pope, C.J. and Howard, J.B., "Simultaneous Particle and Molecule Modeling (SPAMM): An Approach for Combining Sectional Aerosol Equations and Elementary Gas-Phase Reactions," *Aerosol Sci Technol* 27:73-94, 1997.
28. Aubagnac-Karkar, D., Michel, J.-B., Colin, O., Noël, L. et al., "A Sectional Soot Model for RANS Simulation of Diesel Engines," SAE Technical Paper 2014-01-1590, 2014, https://doi.org/10.4271/2014-01-1590.
29. Aubagnac-Karkar, D., Michel, J.-B., Colin, O., Vervisch-Kljakic, P.E. et al., "Sectional Soot Model Coupled to Tabulated Chemistry for Diesel RANS Simulations," *Combust Flame* 162:3081-3099, 2015.
30. Gallen, L., Felden, A., Riber, E., and Cuenot, B., "Lagrangian Tracking of Soot Particles in LES of Gas Turbines," *Proceedings of the Combustion Institute* 37(4):5429-5436, 2019.
31. Dellinger, N., Bertier, N., Dupoirieux, F., and Legros, G., "Hybrid Eulerian-Lagrangian Method for Soot Modelling Applied to Ethylene-Air Premixed Flames," *Energy* 194:116858, 2020.
32. Ong, J.C., Pang, K.M., Walther, J.H., Ho, J.-H. et al., "Evaluation of a Lagrangian Soot Tracking Method for the Prediction of Primary Soot Particle Size under Engine-Like Conditions," *J Aerosol Sci* 115:70-95, 2018.
33. Weller, H.G., Tabor, G., Jasak, H., and Fureby, C., "A Tensorial Approach to Computational Continuum Mechanics Using Object-Oriented Techniques," *Comput Phys* 12:620-631, 1998.
34. ECN, "Engine Combustion Network 2020," www.sandia.gov/ecn/, accessed 20 Aug. 2020.
35. Reitz, R.D. and Diwakar, R., "Effect of Drop Breakup on Fuel Sprays," *SAE Trans.* 1:218-227, 1986.
36. Launder, B.E., and Spalding, D.B., "The Numerical Computation of Turbulent Flows," *Comput Methods Appl Mech Eng* 3:269-289, 1974, https://doi.org/10.1016/0045-7825(74)90029-2.
37. Novella, R., García, A., Pastor, J.M., and Domenech, V., "The Role of Detailed Chemical Kinetics on CFD Diesel Spray Ignition and Combustion Modelling," *Math Comput Model* 54:1706-1719, 2011.
38. Pang, K.M., Jangi, M., Bai, X.-S., and Schramm, J., "Investigation of Chemical Kinetics on Soot Formation Event of n-Heptane Spray Combustion," SAE Technical Paper 2014-01-1254, 2014, https://doi.org/10.4271/2014-01-1254.
39. Pang, K.M., Jangi, M., Bai, X.-S., and Schramm, J., "Evaluation and Optimisation of Phenomenological Multi-Step Soot Model for Spray Combustion under Diesel Engine-Like Operating Conditions," *Combust Theory Model* 19:279-308, 2015.
40. Varna, A., Wehrfritz, A., Hawkes, E.R., Cleary, M.J. et al., "Application of a Multiple Mapping Conditioning Mixing Model to ECN Spray A," *Proceedings of the Combustion Institute* 37(3):3263-3270, 2019.
41. Skeen, S., Manin, J., Pickett, L., Dalen, K. et al., "Quantitative Spatially Resolved Measurements of Total Radiation in High-Pressure Spray Flames," SAE Technical Paper 2014-01-1252, 2014, https://doi.org/10.4271/2014-01-1252.
42. Jangi, M., D'Errico, G., Bai, X.-S., and Lucchini, T., "Numerical Simulation of the ECN Spray A Using Multidimensional Chemistry Coordinate Mapping: n-Dodecane Diesel Combustion," SAE Technical Paper 2012-01-1660, 2012, https://doi.org/10.4271/2012-01-1660.
43. Ranz, W.E. and Marshall, W.R., "Evaporation from Drops," *Chem Eng Prog* 48:141446, 1952.
44. Frossling, N., "Evaporation, Heat Transfer, and Velocity Distribution in Two-Dimensional and Rotationally Symmetrical Laminar Boundary-Layer Flow," DTIC Document, 1956.

45. Pang, K.M., Ng, H.K., and Gan, S., "Development of an Integrated Reduced Fuel Oxidation and Soot Precursor Formation Mechanism for CFD Simulations of Diesel Combustion," *Fuel* 90:2902-2914, 2011.
46. Kitanidis, P.K., "Particle-Tracking Equations for the Solution of the Advection-Dispersion Equation with Variable Coefficients," *Water Resour Res* 30:3225-3227, 1994.
47. Zhang, Z. and Chen, Q., "Comparison of the Eulerian and Lagrangian Methods for Predicting Particle Transport in Enclosed Spaces," *Atmos Environ* 41:5236-5248, 2007.
48. Bolla, M., Wright, Y.M., Boulouchos, K., Borghesi, G. et al., "Soot Formation Modeling of n-Heptane Sprays under Diesel Engine Conditions Using the Conditional Moment Closure Approach," *Combustion Science and Technology* 185(5):766-793, 2013.
49. Haynes, B.S. and Wagner, H.G., "The Surface Growth Phenomenon in Soot Formation," *Zeitschrift für Physikalische Chemie* 133(2):201-213, 1982.
50. Brookes, S.J. and Moss, J.B., "Predictions of Soot and Thermal Radiation Properties in Confined Turbulent Jet Diffusion Flames," *Combust Flame* 116:486-503, 1999.
51. Ong, J.C., "Development of Lagrangian Soot Tracking Method for the Study of Soot Morphology in Diesel Spray Combustion," Ph.D. thesis, University of Nottingham, 2017.
52. Leung, K.M., Lindstedt, R.P., and Jones, W.P., "A Simplified Reaction Mechanism for Soot Formation in Nonpremixed Flames," *Combust Flame* 87:289-305, 1991.
53. Vishwanathan, G. and Reitz, R.D., "Development of a Practical Soot Modeling Approach and Its Application to Low-Temperature Diesel Combustion," *Combust Sci Technol* 182:1050-1082, 2010.
54. Katta, V.R., Blevins, L.G., and Roquemore, W.M., "Dynamics of an Inverse Diffusion Flame and Its Role in Polycyclic-Aromatic-Hydrocarbon and Soot Formation," *Combust Flame* 142:33-35, 2005.
55. Pei, Y., Som, S., Pomraning, E., Senecal, P.K. et al., "Large Eddy Simulation of a Reacting Spray Flame with Multiple Realizations under Compression Ignition Engine Conditions," *Combustion and Flame* 162(12):4442-4455, 2015.
56. Fernandez, S.F., Paul, C., Sircar, A., Imren, A. et al., "Soot and Spectral Radiation Modeling for High-Pressure Turbulent Spray Flames," *Combustion and Flame* 190:402-415, 2018.
57. Chishty, M.A., Bolla, M., Hawkes, E.R., Pei, Y. et al., "Soot Formation Modelling for n-Dodecane Sprays Using the Transported PDF Model," *Combustion and Flame* 192:101-119, 2018.
58. Idicheria, C.A. and Pickett, L.M., "Soot Formation in Diesel Combustion under High-EGR Conditions," *SAE Trans.* 114(4):1559-1574, 2005, https://doi.org/10.4271/2005-01-3834.
59. Cenker, E., "Imaging Measurements of Soot Particle Size and Soot Volume Fraction with Laser-Induced Incandescence at Diesel Engine Conditions," PhD thesis, Ecole Centrale Paris, 2014.
60. Pandurangi, S.S., Bolla, M., Wright, Y.M., Boulouchos, K. et al., "Onset and Progression of Soot in High-Pressure n-Dodecane Sprays under Diesel-Engine Conditions," *Int J Engine Res.* 18(5-6):436-452, 2017.
61. Kook, S., Zhang, R., Chan, Q.N., Aizawa, T. et al., "Automated Detection of Primary Particles from Transmission Electron Microscope (TEM) Images of Soot Aggregates in Diesel Engine Environments," *SAE Int. J. Engines* 9(1):279-296, 2016, https://doi.org/10.4271/2015-01-1991.
62. Pickett, L.M. and Siebers, D.L., "Soot in Diesel Fuel Jets: Effects of Ambient Temperature, Ambient Density, and Injection Pressure," *Combust Flame* 138:114-135, 2004.
63. Oh, K.C. and Shin, H.D., "The Effect of Oxygen and Carbon Dioxide Concentration on Soot Formation in Non-premixed Flames," *Fuel* 85:615-624, 2006.
64. Vargas, A.M. and Gülder, Ö.L., "Pressure Dependence of Primary Soot Particle Size Determined Using Thermophoretic Sampling in Laminar Methane-Air Diffusion Flames," *Proc Combust Inst* 36:975-984, 2017.
65. Amin, H.M.F. and Roberts, W.L., "An Experimental Apparatus to Measure Soot Morphology at High Pressures Using Multi-Angle Light Scattering," *Meas Sci Technol* 30:75902, 2019.
66. Amin, H.M.F. and Roberts, W.L., "Investigating Soot Parameters in an Ethane/Air Counterflow Diffusion Flame at Elevated Pressures," *Combust Sci Technol* 1-16, 2020.
67. Singh, J., Balthasar, M., Kraft, M., and Wagner, W., "Stochastic Modeling of Soot Particle Size and Age Distributions in Laminar Premixed Flames," *Proc Combust Inst* 30:1457-1465, 2005.